THE INTERNAL SHEAR OF TYPE Ia SUPERNOVA PROGENITORS DURING ACCRETION AND SIMMERING

Anthony L. Piro

Astronomy Department and Theoretical Astrophysics Center, 601 Campbell Hall, University of California,
Berkeley, CA 94720; tpiro@astro.berkeley.edu

ABSTRACT

A white dwarf (WD) gains substantial angular momentum during the accretion process that grows it toward a Chandrasekhar mass. It is therefore expected to be rotating quickly when it ignites as a Type Ia supernova. The thermal and shearing profiles are important for subsequent flame propagation. We highlight processes that could affect the WD shear during accretion, as well as during the ~ 1000 yr of pre-explosive simmering. Baroclinic instabilities and/or the shear growth of small magnetic fields provide sufficient torque to bring the WD very close to solid-body rotation during accretion. The lack of significant shear makes it difficult to grow a WD substantially past the typical Chandrasekhar mass. Once carbon ignites, a convective region spreads from the center of the WD. This phase occurs regardless of progenitor scenario, and therefore it is of great interest for understanding how the WD interior is prepared before the explosive burning begins. We summarize some of the key properties of the convective region, including a demonstration that the mass enclosed by convection at any given time depends most sensitively on a single parameter that can be expressed as either the ratio of temperatures or densities at the top and bottom of the convection zone. At low Rossby numbers, the redistribution of angular momentum by convection may result in significant shearing at the convective/nonconvective boundary.

Subject headings: accretion, accretion disks — convection — hydrodynamics — stars: magnetic fields — white dwarfs

1. INTRODUCTION

The fundamental role played by Type Ia supernovae (SNe Ia) in determining the expansion history of the universe (Riess et al. 2004 and references therein) has added new urgency to understanding the progenitors of these events. Theoretical work on modeling the flame dynamics of exploding white dwarfs (WDs) has demonstrated that the composition and energy of ejecta depend sensitively on the competition between flame propagation, instabilities driven by turbulence, and expansion of the WD (e.g., Hillebrandt & Niemeyer 2000). This has sparked new interest in understanding the evolution that occurs up until the onset of explosive burning. A critical aspect is the shear profile present within the WD.

SNe Ia are expected to occur exclusively in accreting binary systems. Therefore, the role of angular momentum may be unique or at least especially important for these SNe. If accretion drives shear in the WD, it may be an important source of viscous heating and material mixing. Yoon & Langer (2004) considered the accretion and evolution of a WD up until the point of ignition, including the effects of rotation. In their study, angular momentum was transported primarily via the Kelvin-Helmholtz instability, which led to significant shear throughout the WD. Saio & Nomoto (2004) focused on whether rotational effects can prevent accretion-induced collapse (AIC) at high accretion rates $[\dot{M} = (3 \times 10^{-6})-(1 \times 10^{-5})\, M_\odot\, \mathrm{yr}^{-1}]$. They found that an AIC was not averted, but, perhaps more interestingly, they also found that the WD should be rotating nearly uniformly when the baroclinic instability is included, a process that was neglected by Yoon & Langer (2004).

There is further opportunity for shear to develop during the carbon simmering phase. At carbon ignition, a convective region grows at the WD center. This envelops $\sim 1\, M_\odot$ over a timescale of ~ 1000 yr, until a burning wave commences. This phase has received increasing attention in recent years due to the realization that it sets the initial temperature and density for the explosive burning (Lesaffre et al. 2006), as well as the distribution of ignition points (Woosley et al. 2004; Wunsch & Woosley 2004; Kuhlen et al. 2006). Nuclear reactions during this time may change the neutron excess of the WD core, which is crucial for determining the ratio of radioactive to nonradioactive nickel produced in the Type Ia explosion (Piro & Bildsten 2008; Chamulak et al. 2008).

In the present study, we consider the opportunity for developing shear during both of these stages. In § 2, we revisit estimates for the shear of accreting WDs and confirm that the baroclinic instability limits the shear before the Kelvin-Helmholtz instability initiates. In addition, we explore whether magnetohydrodynamic effects could reduce the shear even further. We conclude that the WD is nearly uniformly rotating at the onset of carbon ignition, and that viscous heating is negligible. In § 3, we explore the properties of convection prior to explosive burning. The growth of this convective region allows further opportunity for shearing. The three-dimensional nature of this problem makes it hard to definitively determine what occurs during this stage. We illustrate some general features expected for the interaction of spin and convection by appealing to observations and numerical experiments. In § 4, we conclude with a summary of our results and a discussion of future research.

2. SHEAR PROFILE DURING ACCRETION

Material accreted at a rate $\dot{M}$ reaches the WD surface with a nearly Keplerian spin frequency of $\Omega_K = (GM/R^3)^{1/2}$. The majority of the kinetic energy associated with this flow is dissipated in a boundary layer of thickness $H_{\mathrm{BL}} \ll R$ (as studied by Piro & Bildsten 2004) and never reaches far into the surface. Nevertheless, angular momentum is added at a rate $\dot{M}R^2\Omega_K$, so

a torque of this magnitude should be communicated into the WD. It remains an open question whether all of this angular momentum is ultimately added to the WD. If it were, the WD would reach overcritical rotation well before attaining the conditions necessary for carbon ignition (MacDonald 1979). Feedback with the accretion disk at high spin rates may provide a solution to this problem (Paczyński 1991; Popham & Narayan 1991). Observations of cataclysmic variables show a wide range of rotational velocities, many of which are too low to account for the amount of angular momentum that should have been accreted (Sion 1999). This may be related to the periodic mass loss these systems undergo in classical novae (Livio & Pringle 1998).

For our present study, the viscous mechanisms we consider have viscous timescales ($t_{\rm visc} = H^2/\nu$, where $H = P/\rho g$ is the pressure scale height, $g = GM/r^2$ is the local gravitational acceleration, and ν is the viscosity[1]) that are much shorter than the timescale of accretion, $t_{\rm acc} \sim 10^5$–10^9 yr. Due to this hierarchy of timescales, we expect that the spin at any given moment can be broken into two contributions, which we write as

$$\Omega(r, t) = \Omega_0(t) + \Delta\Omega(r, \Omega_0(t)). \qquad (1)$$

The first piece, $\Omega_0(t)$, represents the solid body rotation of the WD, which is increasing with time as accretion takes place. The second piece, $\Delta\Omega(r, \Omega_0(t))$, is the shear that must be present to transport the accretion torque into the WD. As long as the timescales obey $t_{\rm visc}/t_{\rm acc} \ll 1$, the viscosity is extremely efficient at transporting angular momentum. This means that the shear needed for transport is small, $\Delta\Omega \ll \Omega_0$, and that the shear quickly comes into steady state for a given $\Omega_0(t)$, so that $\Delta\Omega$ does not explicitly depend on t.

Since all of the transport mechanisms we examine operate most efficiently in directions perpendicular to gravity (because no work is performed), it is adequate to consider a structure composed of concentric spheres, each with constant Ω. Transfer of angular momentum is reduced to a one-dimensional diffusion equation (Fujimoto 1993):

$$\frac{\partial}{\partial t}(r^2\Omega) = \frac{1}{r^2\rho}\frac{\partial}{\partial r}\left(\rho\nu r^4 \frac{\partial\Omega}{\partial r}\right). \qquad (2)$$

We substitute equation (1) and assume that r is roughly independent of time to obtain

$$r^2\left(1 + \frac{\partial\Delta\Omega}{\partial\Omega_0}\right)\frac{d\Omega_0}{dt} = \frac{1}{r^2\rho}\frac{\partial}{\partial r}\left(\rho\nu r^4 \frac{\partial\Delta\Omega}{\partial r}\right). \qquad (3)$$

The second term within the parenthesis on the left-hand side is negligible, since it is $\mathcal{O}(\Delta\Omega/\Omega_0) \ll 1$. Multiplying both sides by $4\pi\rho r^2$ and integrating over the radius, we find

$$I(r)\frac{d\Omega_0}{dt} = 4\pi\rho\nu r^4 \frac{\partial\Delta\Omega}{\partial r}, \qquad (4)$$

where we have set the integration constant to zero to assure that the torque vanishes at the center of the WD, and

$$I(r) = \int_0^r 4\pi\rho r^4 dr \qquad (5)$$

[1] This viscosity can represent either a molecular viscosity or a turbulent viscosity, but for the scenarios discussed in § 2.1, a turbulent viscosity is argued to be dominant.

is the moment of inertia interior to a given radius. The rate of change of the WD spin is set by the accretion torque, so that $I_{\rm tot}d\Omega_0/dt = \dot{M}R^2\Omega_{\rm K}$, where $I_{\rm tot} = I(R)$ is the total moment of inertia. This gives us an equation for the shear $\sigma \equiv \partial\Delta\Omega/d\ln r$:

$$\dot{M}R^2\Omega_{\rm K}I(r)/I_{\rm tot} = 4\pi\rho\nu r^3\sigma. \qquad (6)$$

This result reduces to the angular momentum equations presented by Fujimoto (1993) and Piro & Bildsten (2007) in the plane-parallel limit by taking $I(r) \approx I_{\rm tot}$. With this expression, we can now estimate the shear at a given depth as a function of Ω_0 and $\dot{M}$. The advantage of this approach is that Ω_0 can be treated as a free parameter, and we are not restricted to following the full history of angular momentum transport for the WD.

Since for the remainder of § 2 we assume that the approximations presented here hold true, we simplify the notation by using Ω to represent the solid-body rotation rate and σ to represent the shear.

2.1. Summary of Transport Mechanisms

In the following sections, we discuss some of hydrodynamic and magnetohydrodynamic instabilities expected to be present in the shearing WD core. We summarize three distinct eddy diffusivities related to these instabilities and explore their influence on the shear profile. This is not meant to be an exhaustive survey of all possible turbulent angular momentum transport mechanisms. Instead, it is meant to highlight those that have been used in previous studies along with others that have received less attention in the past, but which we show to be important.

2.1.1. Kelvin-Helmholtz Instability

A hydrodynamic instability that has been popular for application to accreting WDs is the Kelvin-Helmholtz instability (see Yoon & Langer 2004 and associated work). This instability is activated when Ri < 1/4, where the Richardson number is

$$\mathrm{Ri} \equiv \frac{N^2}{\sigma^2}, \qquad (7)$$

and N is the Brunt-Väisälä frequency, given by

$$N^2 = \frac{\mathcal{Q}g}{H}\left[\nabla_{\rm ad} - \left(\frac{d\ln T}{d\ln P}\right)_*\right] \qquad (8)$$

(ignoring compositional gradients), where $\mathcal{Q} = -(\partial\ln\rho/\partial\ln T)_P$, $\nabla_{\rm ad} = (\partial\ln T/\partial\ln P)_{\rm ad}$ is the adiabatic temperature gradient, and the asterisk refers to derivatives of the envelope's profile. The electron viscosity is the dominant molecular viscosity in the degenerate WD. Substituting the viscosity from Nandkumar & Pethick (1984) into equation (6) results in a shear in which Ri ≪ 1/4, and thus Kelvin-Helmholtz instability is expected. This confirms the result of Yoon & Langer (2004) that in the absence of other instabilities, Kelvin-Helmholtz instability is dominant, so that we view its associated shear as an upper limit.

Kelvin-Helmholtz instability causes a turbulent eddy diffusivity given by (Fujimoto 1993)

$$\nu_{\rm KH} = \frac{(1 - 4\mathrm{Ri})^{1/2}}{2\mathrm{Ri}^{1/2}}H^2N. \qquad (9)$$

Since it only acts for Ri < 1/4, it causes the shearing to evolve until Ri = 1/4 is marginally satisfied. Thus, it is a good approximation to estimate the shear to be $\sigma_{\rm KH} \approx 2N$ when secular instabilities due to thermal diffusion can be neglected (e.g., Zahn

1992), as is the case for the conductive WD core. Since electron degeneracy provides the dominant pressure, we approximate the Brunt-Väisälä frequency as

$$N \approx \left(\frac{g}{H}\frac{k_B T}{Z E_F}\right)^{1/2}, \tag{10}$$

where k_B is Boltzmann's constant, Z is the charge per ion, and E_F is the Fermi energy for a degenerate, relativistic electron gas. We estimate for Kelvin-Helmholtz-driven shear,

$$\sigma_{KH} \approx 0.5 \text{ s}^{-1} \; g_{10}\left(\frac{\mu_e}{2}\right)^{5/6}\left(\frac{6}{Z}\right)^{1/2}\frac{T_8^{1/2}}{\rho_9^{1/3}}, \tag{11}$$

where $g_{10} = g/10^{10}$ cm s^{-2}, μ_e is the mean molecular weight per electron, $\rho_9 = \rho/10^9$ g cm^{-3}, and $T_8 = T/10^8$ K. This result is in reasonable agreement with the detailed, time-dependent simulations by Yoon & Langer (2004).

2.1.2. Baroclinic Instability

Another hydrodynamic instability that may be important is the baroclinic instability (Fujimoto 1987, 1988; see also Cumming & Bildsten 2000). This instability arises because surfaces of constant pressure and density no longer coincide when hydrostatic balance is maintained under differential rotation. In such a configuration, fluid perturbations along nearly horizontal directions are unstable, although they have a radial component sufficient to allow mixing of angular momentum and material. When Ri is greater than the critical baroclinic Richardson number (Fujimoto 1987),

$$\text{Ri}_{BC} \equiv 4\left(\frac{r}{H}\right)^2\left(\frac{\Omega}{N}\right)^2, \tag{12}$$

Coriolis effects limit the horizontal scale of perturbations, and the associated turbulent viscosity is approximated from linear theory to be (Fujimoto 1993)

$$\nu_{BC} = \frac{1}{3}\frac{\text{Ri}_{BC}}{\text{Ri}^{3/2}}H^2\Omega. \tag{13}$$

In the WD interior, $\text{Ri}_{BC} \sim 10$, whereas the Richardson number found for $\nu = \nu_{BC}$ (using eqs. [6] and [7]) is Ri $\sim 10^6$; thus, the limit Ri $\gg \text{Ri}_{BC}$ is clearly satisfied.

The Richardson number can be estimated by combining equations (6), (7), and (13), giving

$$\text{Ri}^2 = \frac{16\pi}{3}\frac{\rho r^3 \Omega}{\dot{M}}\left(\frac{r}{R}\right)^2\frac{\Omega}{\Omega_K}\frac{\Omega}{N}\frac{I_{tot}}{I(r)}. \tag{14}$$

To illustrate how the shear depends on the properties of the interior, we take

$$\frac{16\pi}{3}\frac{\rho r^3 \Omega}{\dot{M}} \sim \frac{t_{acc}}{t_{dyn}}\frac{\Omega}{\Omega_K}\left(\frac{r}{R}\right)^3, \tag{15}$$

where $t_{acc} = M/\dot{M}$ is the accretion timescale, and $t_{dyn} = \Omega_K^{-1}$ is the dynamical time. Using $\sigma_{BC} = N/\text{Ri}^{1/2}$ and $I(r)/I_{tot} \sim (r/R)^5$, we estimate

$$\sigma_{BC} \sim 10^{-4} \text{ s}^{-1} \left(\frac{t_{acc}/t_{dyn}}{10^{15}}\right)^{-1/4}\left(\frac{\Omega/\Omega_K}{0.1}\right)^{-1/2}$$

$$\times \left(\frac{N}{\Omega}\right)^{1/4}\left(\frac{N}{0.3 \text{ s}^{-1}}\right). \tag{16}$$

In § 2.2.1, we show that the timescale for viscous diffusion from the baroclinic instability is much shorter than the timescale over which accretion takes place. This means that this instability is able to quickly redistribute angular momentum as it accretes, and that the steady state limit will be reached. Coupling this fact to the inequality $\sigma_{BC} \approx \sigma_{KH}/(2\text{Ri}) \ll \sigma_{KH}$ as demonstrated above, we conclude that the baroclinic instability will limit the growth of shear long before the Kelvin-Helmholtz instability can become active. This is consistent with the results of Saio & Nomoto (2004), who included both the Kelvin-Helmholtz instability and the baroclinic instability and found nearly solid-body rotation throughout the WD, even for accretion rates as high as $10^{-5} M_\odot$ yr^{-1}.

2.1.3. Tayler-Spruit Dynamo

The last case we consider is magnetohydrodynamic instabilities, for which we apply the Tayler-Spruit dynamo (Spruit 2002). In this picture, shearing stretches any small component of poloidal magnetic field into a strong toroidal field. Once sufficiently large, the toroidal field initiates Tayler instabilities (nonaxisymmetric, pinchlike instabilities including stratification; Tayler 1973; Spruit 1999), which turbulently create poloidal field components that once again shear to be toroidal. This cycle continues and results in a steady state field that transmits angular momentum via Maxwell stresses. In the limit when the magnetic diffusivity, η, is much less than the thermal diffusivity, K, the minimum shear needed for this process to activate is (Spruit 2002)

$$\sigma_{TS,crit} = \left(\frac{N}{\Omega}\right)^{7/4}\left(\frac{\eta}{r^2 N}\right)^{1/4}\left(\frac{\eta}{K}\right)^{3/4}\Omega. \tag{17}$$

When $\sigma > \sigma_{TS,crit}$, the effective viscosity due to the steady state magnetic fields is

$$\nu_{TS} = r^2\Omega\left(\frac{\Omega}{N}\right)^{1/2}\left(\frac{K}{r^2 N}\right)^{1/2}. \tag{18}$$

We wait until the following section to present the shear associated with this process.

2.2. Comparison Calculations

We now calculate the isothermal WD profiles and the shear profiles for the mechanisms described above. Such models allow us to argue that *solid-body rotation* is the most likely result.

The WD models are computed by solving for hydrostatic balance with the effects of spin ignored, since we generally consider spins on the order of $0.1\Omega_K$. We solve for ρ using the analytic equation of state from Paczyński (1983). The importance of Coulomb interactions is measured by the parameter

$$\Gamma = \frac{(Ze)^2}{ak_B T} = 35.7\frac{\rho_9^{1/3}}{T_8}\left(\frac{Z}{6}\right)^2\left(\frac{12}{A}\right)^{1/3}, \tag{19}$$

where A is the mass per ion, and a is the ion separation. For the liquid phase, when $1 \le \Gamma \le 173$, we include the ionic free energy of Chabrier & Potekhin (1998). The composition is set to 50% ^{12}C, 48% ^{16}O, and 2% ^{22}Ne by mass.

In Figure 1, we compare the shear rates found by calculating the effects of each viscous mechanism individually. In addition, we plot the critical shear required for the Tayler-Spruit dynamo to be activated, $\sigma_{TS,crit}$ (eq. [17]). All models use an isothermal temperature of $T_i = 10^8$ K and a WD mass of $1.37 M_\odot$ (i.e., near
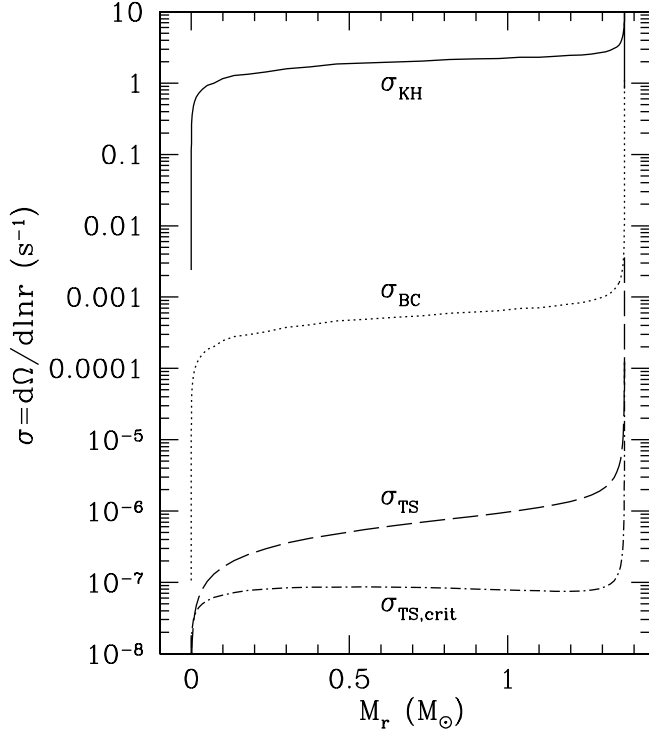
Fig. 1.—Comparison of the shear rate associated with three different viscous mechanisms as a function of mass coordinate: Kelvin-Helmholtz instability (*solid line*), baroclinic instability (*dotted line*), and the Tayler-Spruit dynamo (*dashed line*). We also plot the critical shear rate needed for the Tayler-Spruit dynamo to be activated (*dot-dashed line*). The WD is isothermal, with $T_i = 10^8$ K, $M = 1.37 \, M_\odot$, $\Omega = 0.1$, $\Omega_K = 0.67$ s^{-1}, and $\dot{M} = 10^{-7} \, M_\odot$ yr^{-1}.

Fig. 2.—Estimates of B_ϕ (*solid line*) and B_r (*dashed line*) as implied by the Tayler-Spruit dynamo using the same WD model from Fig. 1. The fields associated with other accretion rates and spins can be estimated using $B_\phi \propto \dot{M}^{1/2}\Omega^{-1/8}$ and $B_r \propto \dot{M}^{1/2}\Omega^{1/8}$ (Piro & Bildsten 2007). Plotted for $H/r < 1/2$ is $B_{\rm buoy}$ (*dotted line*), which is the critical field needed for the buoyancy instability to occur (eq. [21]).

the critical mass for carbon ignition). We calculate $\sigma_{\rm KH}$ using the approximation $\sigma_{\rm KH} \approx 2N$. Both $\sigma_{\rm BC}$ and $\sigma_{\rm TS}$ are calculated by substituting their associated viscosities into equation (6) and solving for the shear using $\Omega = 0.1\Omega_K = 0.67$ s^{-1} and $\dot{M} = 10^{-7} \, M_\odot$ yr^{-1}.

Although the structure of an accreting WD is not exactly isothermal due to the competition of compression and cooling (for example, Nomoto 1982), we can still make many conclusions using our simple model. Both $\sigma_{\rm KH}$ and $\sigma_{\rm BC}$ are consistent with what we estimated analytically. In fact, $\sigma_{\rm KH}$ has a value within a factor of a few of what Yoon & Langer (2004) found for detailed accreting models (see their Fig. 7). Our calculations demonstrate that the baroclinic instability does not allow the shear to grow sufficiently for the Kelvin-Helmholtz instability to ever be important. Since $\sigma_{\rm BC} \ll \Omega$, the WD should exhibit nearly solid-body rotation. Also, note that this is for $\Omega = 0.1\Omega_K$. Larger spins result in even smaller shear, since $\sigma_{\rm BC} \propto \Omega^{-3/4}$ (eq. [16]). This is because at higher Ω, the relative amount of specific angular momentum in the disk versus the WD surface is smaller.

We also consider the Tayler-Spruit dynamo in Figure 1. The thermal diffusivity is given by $K = 16\sigma_{\rm SB}T^3/(3c_p\kappa\rho^2)$, where $\sigma_{\rm SB}$ is the Stefan-Boltzmann constant, c_p is the specific heat capacity at constant pressure, and κ is the opacity. For the opacity, we include electron scattering (Paczyński 1983), free-free, and conductive contributions (Schatz et al. 1999). The magnetic diffusivity is set as $\eta = \pi k_{\rm B}^2 Tc^2/(12e^2 K_c)$, where K_c is the conductivity from Schatz et al. (1999). The prescriptions given by Spruit (2002) imply an even smaller shear rate than the baroclinic instability. Associated with this small shear are steady state radial and azimuthal magnetic fields, which we plot in Figure 2. This confirms that $B_r/B_\phi \ll 1$, which is ex-
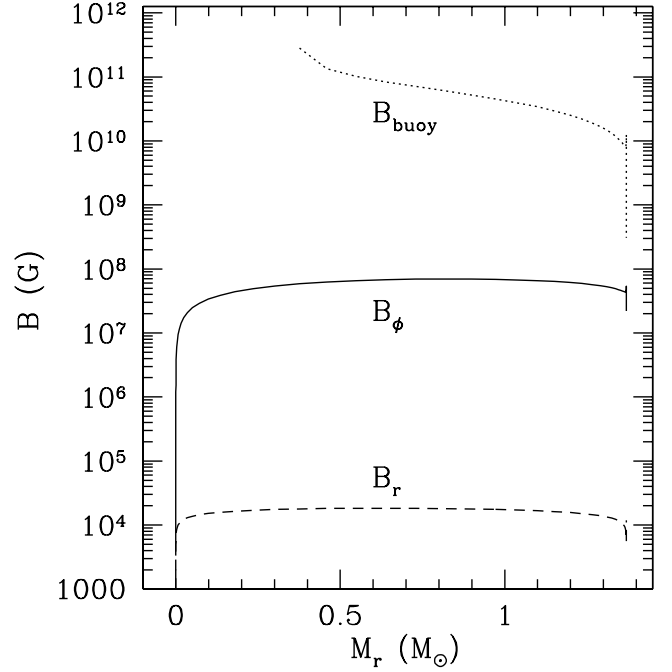
pected because the toroidal field growth is driven by shearing. The convection associated with the simmering phase (as studied in § 3) may destroy this magnetic field for $M_r \lesssim 1 \, M_\odot$, but the field within the convectively stable region will remain. Whether or not these fields are important for the later flame propagation when the WD is incinerated or for observations of SNe Ia is an interesting question. According to Piro & Bildsten (2007), both B_r and $B\phi \propto \dot{M}^{1/2}$ for the Tayler-Spruit dynamo. Thus, any process or observational diagnostic that is sensitive to the magnetic field strength would reveal something about $\dot{M}$, an important discriminant between progenitor models.

There is uncertainty in applying the Tayler-Spruit formulae to the case of an accreting WD. In the analysis presented by Spruit (2002), it is assumed that $N > \Omega > \omega_{\rm A}$, where $\omega_{\rm A} = B/[(4\pi\rho)^{1/2}r]$ is the Alfvén frequency. Such inequalities are appropriate for the radiative interior of the Sun (for which this work was originally motivated). In the WD interior it is possible that $\Omega \gtrsim N$, since the Brunt-Väisälä frequency is decreased by degeneracy effects (eq. [10]). Denissenkov & Pinsonneault (2007) consider the effects of a large spin and find that the effective viscosity of the dynamo is significantly reduced by a factor of $(K/r^2N)^{1/6}(\Omega/N)^{1/6}(\sigma/\Omega)^{2/3} \ll 1$. We hesitate to implement their prescriptions because their results are based on purely heuristic arguments without the rigorous analysis of an appropriate dispersion relation (as was provided in Spruit 2006). Since the baroclinic instability still contributes a large viscosity, our conclusion of solid-body rotation is unchanged.

An interesting possibility is that in the limit of large spin, an instability other than Tayler instability is responsible for turbulently creating the poloidal magnetic field components necessary for closing the dynamo loop. The magnetorotational instability (Velikhov 1959; Chandrasekhar 1960; Fricke 1969; Acheson 1978; Balbus & Hawley 1991, 1992; Balbus 1995) cannot provide closure to the dynamo, since it requires $d\Omega/dr < 0$, which
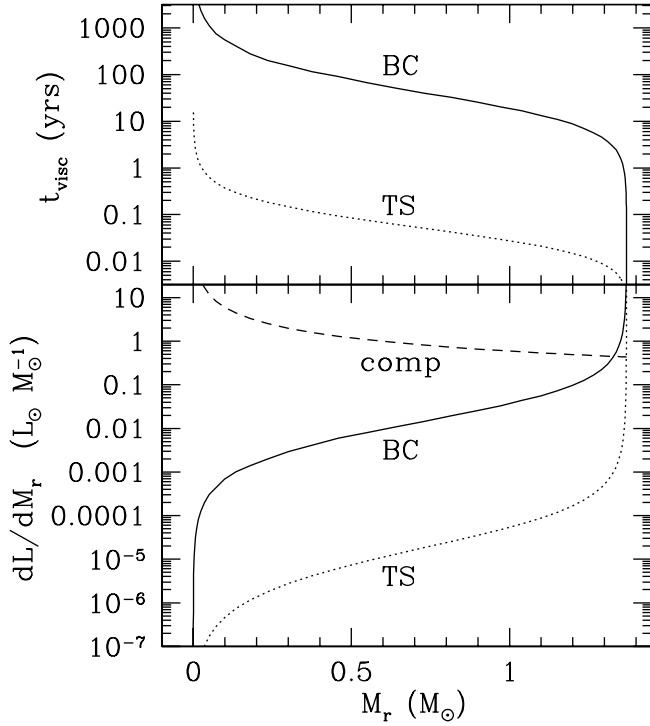
FIG. 3.—*Top*: Comparison of the timescales for viscous transport of angular momentum via the baroclinic instability (*solid line*) and the Tayler-Spruit dynamo (*dotted line*). *Bottom*: Rate of energy generation for both viscous mechanisms, as well as the heating expected from the compression of the WD from accretion (eq. [24]; *dashed line*). The WD models are the same as described in Fig. 1.

is opposite to what is found in the WD interior. For similar reasons, magnetic shear instabilities are also ruled out (Acheson 1978). Since the magnetic fields plotted in Figure 2 decrease with radius near the outer parts of the WD, it is possible that the magnetic buoyancy instability occurs. Using the results from Acheson (1978), Spruit (1999) shows in the limit of $\sigma/\Omega \ll 1$ that such an instability arises for $H/r < 1/2$ when

$$\frac{\eta}{K}\frac{N^2}{\omega_A^2} + \left(\frac{r}{H} - 2\right)\frac{d\ln B}{d\ln r} \lesssim 0, \qquad (20)$$

where we must remember that $d\ln B/d\ln r < 0$. This limit is easiest to interpret if we solve for the magnetic field strength needed to satisfy this inequality, which is

$$B \gtrsim B_{\rm buoy} \equiv \frac{(4\pi\rho)^{1/2}(\eta/K)^{1/2}rN}{(r/H - 2)^{1/2}|d\ln B/d\ln r|}. \qquad (21)$$

This illustrates that the magnetic field must be sufficiently strong in comparison to the stratification (represented by N) for the buoyancy instability to occur. We plot $B_{\rm buoy}$ in Figure 2. Since $B_{\rm buoy} \gg B_\phi$, we conclude that the Tayler instability limits magnetic field growth and not the buoyancy instability. Apparently, even when $\Omega > N$, Tayler instability is the correct magnetohydrodynamic instability for closing the shear-driven dynamo in the core of accreting WDs.

2.2.1. Viscous Timescales and Heating

These WD models provide the local viscous timescale for angular momentum transport, $t_{\rm visc} = \min(H^2, R^2)/\nu$, and the heating provided by viscous dissipation. In the top panel of Figure 3, we plot $t_{\rm visc}$ for the baroclinic instability and the

Tayler-Spruit dynamo. Both are significantly smaller than the accretion timescale; thus our approximations presented at the beginning of § 2 are justified. Compositional discontinuities present a possible barrier to angular momentum transport, which we have ignored since we are focused on the WD core. Piro & Bildsten (2007) show in the case of accreting neutron stars that such compositional changes can inhibit turbulent mixing, but do not alter angular momentum transport other than by introducing a slight spin discontinuity. Our assumption of steady state transport in the core is therefore not affected. Figure 3 shows that there is a clear hierarchy of timescales. If both mechanisms were acting, the Tayler-Spruit dynamo would act rapidly enough to limit the shear before the baroclinic instability becomes important.

The viscous heating per unit mass is

$$\epsilon_{\rm visc} = \frac{1}{2}\nu\sigma^2, \qquad (22)$$

so that the total luminosity is

$$L_{\rm visc} = \int_0^M \epsilon_{\rm visc}\, dM_r. \qquad (23)$$

In the bottom panel of Figure 3, we plot the integrand of this expression, $dL_{\rm visc}/dM_r = \epsilon_{\rm visc}$, for the baroclinic and Tayler-Spruit cases in units of $L_\odot\, M_\odot^{-1}$. We denote the heating in this manner to emphasize that with these units, one can easily "integrate by eye" to determine the total luminosity over any region of the WD. The process of accretion and compression leads to additional heating, which has been studied analytically in Appendix B of Townsley & Bildsten (2004). Using their results, we approximate that within the degenerate core,

$$\frac{dL_{\rm comp}}{dM_r} \approx \frac{3}{5}\frac{k_{\rm B}T}{\mu_i m_p}\frac{\dot{M}}{M_r}, \qquad (24)$$

where μ_i is the mean molecular weight per ion. This is also plotted in the bottom panel of Figure 3 (*dashed line*), which shows that the viscous heating is dwarfed by this compressional heating. Not plotted in Figure 3 is the compressional heating in the nondegenerate envelope. This total integrated contribution to the heating is larger than that of the degenerate core for the accretion rates of interest (Nomoto 1982).

We note that Figure 3 shows a model with $\dot{M} = 10^{-7}\, M_\odot$ yr^{-1}, and that at shallow depths baroclinic heating is merely a factor of a few less than compressional heating. Using the scalings derived in § 2.1.2, we find that $dL_{\rm BC}/dM_r \propto \dot{M}^{5/4}$, whereas $dL_{\rm comp}/dM_r \propto \dot{M}$. Thus, viscous heating from baroclinic instabilities is important when $\dot{M} \gtrsim 10^{-5}\, M_\odot$ yr^{-1}, which was demonstrated in some of the models considered by Saio & Nomoto (2004).

3. THE CONVECTION PHASE AND REDISTRIBUTION OF ANGULAR MOMENTUM

The explosive burning that incinerates the WD in the SN Ia does not begin right at carbon ignition. Instead, the carbon simmers for ∼1000 yr, which we summarize in Figure 4 (see also Woosley et al. 2004; Wunsch & Woosley 2004; Lesaffre et al. 2006). As this stage is important for setting the initial conditions for explosive burning, there has recently been significant progress in modeling it numerically (Höflich & Stein 2002; Kuhlen et al. 2006; Stein & Wheeler 2006; Almgren et al. 2006a, 2006b). For our purposes here, we present simpler models that
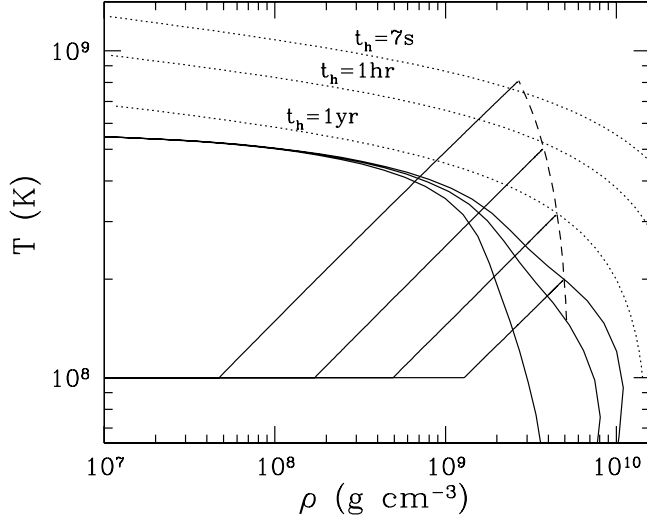
FIG. 4.—Example thermal profiles for a 1.37 $M_\odot$ WD during the simmering phase. Unstable carbon ignition occurs within the range denoted by the thin solid lines (Yakovlev et al. 2006). The thick dashed curve traces the central density and temperature, ignoring compositional changes from the burning. The thick solid lines show example thermal profiles for the WD during different snapshots of the simmering. The nonconvective region is isothermal with $T_i = 10^8$ K. The dotted lines show characteristic heating timescales as labeled.

nonetheless capture many of the crucial features of this stage. For simplicity, we ignore the convective Urca process (Paczyński 1972; Bruenn 1973; Couch & Arnett 1975; Iben 1978a, 1978b, 1982; Barkat & Wheeler 1990; Mochkovitch 1996; Stein et al. 1999; Bisnovatyi-Kogan 2001; Lesaffre et al. 2005; Stein & Wheeler 2006). Ignition first occurs when heating from carbon burning beats neutrino cooling. This is plotted as thin solid lines that show the range of theoretical ignition curves expected for a uniform composition of ^{12}C and ^{16}O, with the middle line giving the optimal result (Yakovlev et al. 2006).

Simmering is followed by calculating a series of hydrostatic WD models, each with a different central temperature, but with a fixed mass of 1.37 $M_\odot$. We use the same microphysics and composition as in § 2.2 and ignore the compositional changes due to the burning. The thick dashed line on the right in Figure 4 traces out the central temperature as a function of density as the simmering takes place. The density decreases as the WD is heated and expands. The thick solid lines show example profiles demonstrating how the convection grows as the central temperature increases. Since the thermal conduction timescale is so long ($\sim 10^6$ yr), the convection is very efficient, and the convective profile is nearly an adiabat. The adiabatic index depends sensitively on the fact that the ions are in a highly correlated liquid state (Townsley & Bildsten 2004):

$$\left(\frac{d\ln T}{d\ln\rho}\right)_{ad} \approx \frac{0.91 + 0.14\Gamma^{1/3}}{1.22 + 0.41\Gamma^{1/3}}, \qquad (25)$$

where Γ is the parameter defined in § 2.2. For the range of models we consider, we find $(d\ln T/d\ln\rho)_{ad} \approx 0.49$–$0.52$ (roughly consistent with Woosley et al. 2004), instead of the usual $\approx 2/3$ that would be appropriate if the ions were an ideal gas. The top of the convective region is set by when it reaches the isothermal temperature of $T_i = 10^8$ K, in other words, where its entropy matches that of the initial thermal profile (Höflich & Stein 2002).

Also plotted in Figure 4 are dotted lines that show characteristic values for the heating timescale, $t_h = c_p T/\epsilon$, where ϵ is the energy generation rate for carbon burning from Caughlan & Fowler (1988), with strong screening included according to Salpeter & van Horn (1969). This gives a rough estimate of the time until the burning wave commences. For the majority of the simmering stage, the true timescale to heat the convective region is significantly longer because the heat capacity of the entire convective zone must be taken into account (see the discussion in Piro & Chang 2008). The deflagration begins once $t_h \sim t_{conv}$, where

$$t_{conv} = \min(H, R_{conv})/V_{conv}, \qquad (26)$$

is the convective overturn timescale, V_{conv} is the characteristic convective velocity, and we have used a mixing length equal to the minimum of either the pressure scale height, H, or the radius of the convective core, R_{conv}. The *exact* condition required for the deflagration to begin depends on what fraction of the convective zone is still responding to the energy input and on the extreme temperature sensitivity of carbon burning ($\epsilon \propto T^{23}$; Woosley et al. 2004). For this reason, Lesaffre et al. (2006) explore $t_{conv} = \alpha t_h$, where $\alpha \lesssim 1$ parameterizes this uncertainty. Since we are only roughly concerned with resolving the end of the simmering phase, we take $t_{conv} \approx t_h$ to find that simmering should end when $t_h \approx 7$ s, at a central temperature and density of $T_c \approx 7.8 \times 10^8$ K and $\rho_c \approx 2.6 \times 10^9$ g cm^{-3}. This is roughly in agreement with the estimates presented by Woosley et al. (2004) using the Kepler stellar evolution code (Weaver et al. 1978).

The series of events that takes place during the simmering phase is expected to occur regardless of the progenitor scenario under consideration, as long as ignition occurs near the center of the WD. Therefore, it is important to study any processes that may influence the subsequent explosive burning of the SN Ia. In the following sections, we describe some of the main characteristics of the convective region, with a focus on its mass and the velocities of convective eddies. Afterward, we estimate how angular momentum may be redistributed by the convection.

3.1. Properties of the Simmering Core

3.1.1. Convective Core Mass

The boundary between the convective and nonconvective zones reaches out to densities as shallow as $\sim 10^7$–10^8 g cm^{-3} (Fig. 4) and encompasses a mass of $M_{conv} \sim 0.9$–1.2 $M_\odot$. Even though the exact transitional depth depends sensitively on the WD's isothermal temperature, as well as on the composition and microphysics near the boundary (Piro & Chang 2008), it is useful to estimate M_{conv}.

In order to gain some intuition for the expected dependencies, we solved for M_{conv} using the Lane-Emden equation for a polytrope of index 3 in the limit of small radius. This showed us that M_{conv} depends on only two parameters: the mean molecular weight, μ_e, and the ratio of the isothermal and central temperatures, T_i/T_c.

Unfortunately, this analytic result cannot be directly applied to the problem at hand to estimate M_{conv} (because the small radius limit is not accurate). We therefore search for the true dependence numerically. In Figure 5, we plot M_{conv} versus T_i/T_c for four different models that sample a range of central densities and isothermal temperatures. This shows that the relation is indeed very tight. A fit to the solid line in Figure 5 gives

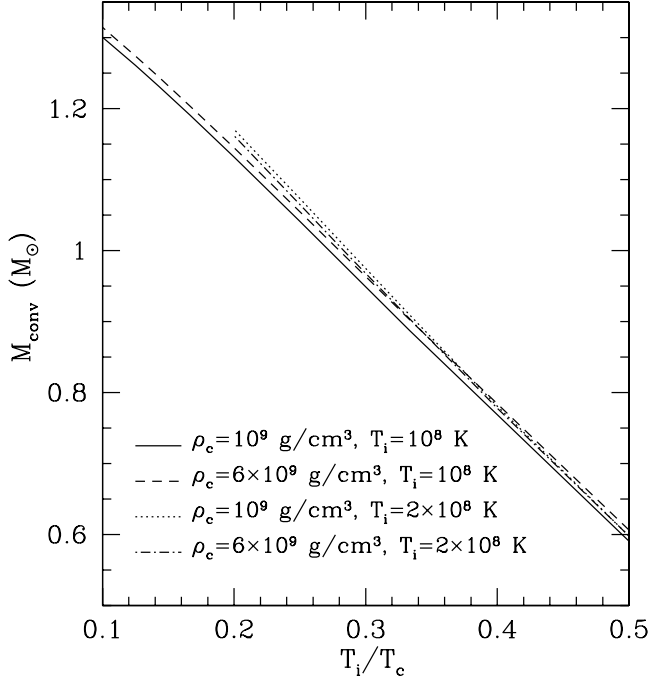$$M_{conv} = 1.48\ M_\odot \left(\frac{2}{\mu_e}\right)^2 \left(1 - 1.20\frac{T_i}{T_c}\right). \qquad (27)$$

FIG. 5.—Mass of the convective core, M_{conv}, as a function of the ratio of the isothermal and central temperatures, T_i/T_c. We consider models with a range of central densities, ρ_c, and isothermal temperatures, T_i, as labeled within the plot. All models trace out a similar relation, which demonstrates that $M_{conv} = M_{conv}(T_i/T_c)$ is a good approximation.

This result could also be written as a ratio of densities, since the convective zone follows an adiabat with approximately $\rho \propto T^2$. Changes in μ_e are primarily due to ^{22}Ne, which gives a range $\mu_e \approx 2.00$–2.01 for a mass fraction range $X(^{22}$Ne$) = 0.00$–0.06. Therefore, μ_e can change M_{conv} by less than 1%. We note that we have omitted an important complication, the presence of gradients in the C/O abundances (e.g., Lesaffre et al. 2006).

This result (eq. [27]) is maybe not too surprising. It is well known that for a relativistic, degenerate equation of state, the characteristic mass of a self-gravitating object (the Chandrasekhar mass) is independent of the central density and only depends on μ_e. In addition, nuclear reactions during the simmering may also complicate things, a possibility that we have ignored. Nevertheless, it is an important relation to keep in mind. It tells us that at any given time, the M_{conv} of a SN Ia progenitor depends most strongly on just a single dimensionless number, and is independent of the progenitor's complicated previous history during the simmering phase.

3.1.2. Convective Velocities

Along with the size of the convective zone, another important property is the speed of the convective eddies. Using estimates from mixing-length theory, the characteristic convective velocity, V_{conv}, is related to F_{conv} for efficient convection via (Hansen & Kawaler 1994)

$$F_{conv} = \frac{c_p T}{Q g H} \rho V_{conv}^3 \approx \rho V_{conv}^3, \qquad (28)$$

where we have used a mixing length that is equal to the scale height, H. If the convective region were static during simmering, then F_{conv} would simply be equal to the integrated nuclear energy generation. Instead, the convection zone is growing, and
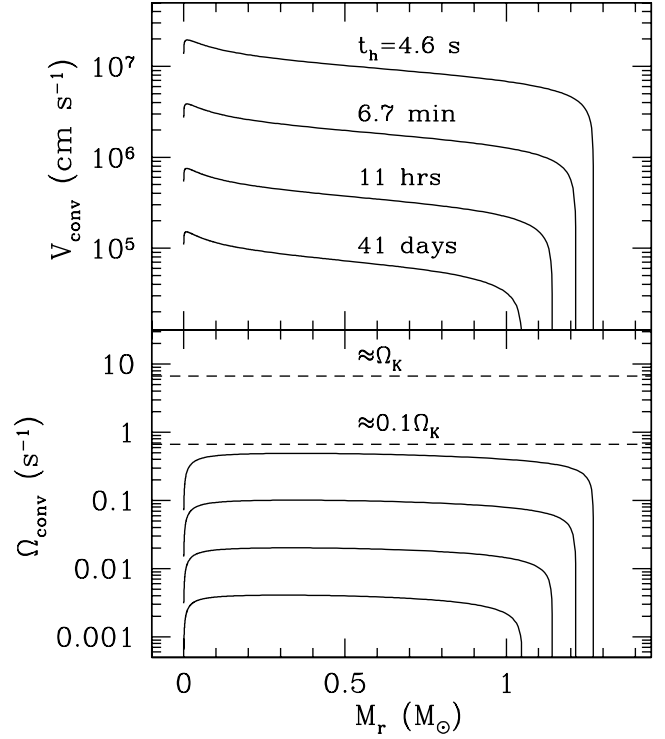

FIG. 6.— *Top*: Plot of the characteristic convective velocity, V_{conv}, as a function of mass coordinate for various times during the simmering phase. Each line is labeled by the heating timescale, $t_h = c_p T/\epsilon$, which is meant as a rough estimate for the time until the deflagration begins. *Bottom*: Plot of the convective eddy turnover frequency, $\Omega_{conv} = t_{conv}^{-1}$ (eq. [26]), for the same four models. The dashed lines denote a reasonable range for the WD spin $\Omega \approx (0.1$–$1.0)\Omega_K$.

energy must be expended to heat new material. Also, the convective flux must be nearly 0 at the convective boundary because of the long conductive timescale here ($\sim 10^6$ yr). These effects cause a decreased F_{conv} in the outer parts of the convective region, which we investigate in more detail in a separate study (Piro & Chang 2008). We borrow these results for presenting V_{conv} here.

In the upper panel of Figure 6, we plot V_{conv} as a function of mass coordinate using equation (28). The characteristic value of $V_{conv} \sim 10^7$ cm s^{-1} during the late stages of convection is consistent with the analytic estimates of Woosley et al. (2004). The turbulent conditions prepared in the core will be important for understanding the subsequent propagation of bubbles and burning. For example, Zingale & Dursi (2007) show that the turbulence may act as a viscous drag that has the largest effect on the smallest bubbles. Another interesting feature is that the material above the convection is devoid of this turbulence. The burning properties could change significantly as a flame passes into this relatively "quiet" region.

The importance of the WD spin for the convection is determined by the convective Rossby number

$$\text{Ro} = \Omega_{conv}/\Omega, \qquad (29)$$

where $\Omega_{conv} = t_{conv}^{-1}$ (see eq. [26]) is the eddy turnover frequency. In the bottom panel of Figure 6, we plot Ω_{conv} along with the expected range of spins relevant for SN Ia progenitors (*dotted lines*). For the entirety of the simmering stage, we find Ro $\lesssim 1$, showing that spin should have a non-negligible influence on the convection (for example, see Kuhlen et al. 2006). This will be an important consideration in the following sections.
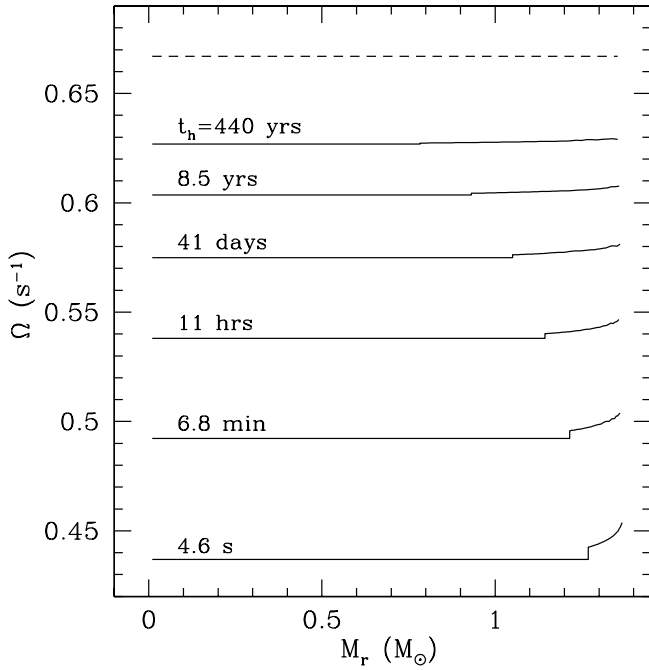
FIG. 7.—Rotation profile vs. mass coordinate for various times during the simmering stage, assuming that uniform rotation is enforced within the convective zone. Each curve is labeled by its associated heating timescale, t_h. The initial spin is taken to be $\Omega = 0.1\Omega_K = 0.67 \text{ s}^{-1}$ (*dashed line*), with a mass of $1.37 \, M_\odot$.

FIG. 8.—Spin *along the equator* vs. mass coordinate assuming a rotation law within the convective zone given by eq. (30) and using the same background models as Fig. 7.

3.2. Rotation Profiles during Simmering

We next consider how the spin changes as convection grows in the core. For the 10^5–10^9 yr that accretion takes place, we have shown that hydrodynamic or magnetohydrodynamic instabilities severely limit shearing. During the last stages of simmering, the WD is changing on the timescale of hours to minutes, so these viscosities will have less influence, and stronger shearing is possible.

Given the conclusions made in § 2, we consider uniform rotation to be a reasonable starting point for when carbon first ignites. Heating and expansion generally cause the WD to spin down (like the freshman physics figure skater problem). In the following calculations, we assume that angular momentum is conserved locally on spherical mass shells in nonconvective regions. The mixing by convective eddies is important for determining the spin within the convective core. Such effects are difficult to estimate, so we consider two possible rotation laws.

3.2.1. Uniform Spin within the Convection

The first rotation law we explore states that convection enforces solid-body rotation. This is the simplest and most naïve assumption one can use. The study by Kumar et al. (1995) argues that such a rotation law is reasonable when convective eddies scatter elastically. Unfortunately, it is not clear whether such a picture of the eddies as separate fluid elements is appropriate. Elastic scattering is, in fact, counter to the standard assumption in mixing-length theory that eddies deposit their entire angular momentum and entropy into the ambient fluid with each scattering. This result also assumes an isotropic scattering, whereas rotation clearly breaks this symmetry. In the anisotropic case, Kumar et al. (1995) find that in principle, angular momentum can be transferred outward by convection, an idea we consider in more detail in the next section.

In Figure 7, we plot the evolution of the WD spin during the simmering stage, assuming solid-body rotation within the convective zone. The initial spin is taken to be uniform with $\Omega = 0.67 \text{ s}^{-1}$
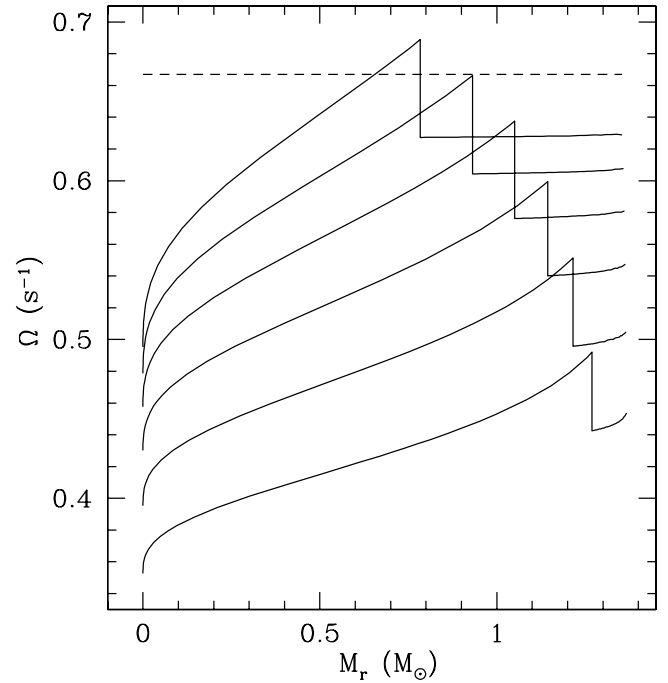
(*dashed line*). The overall trend is spin-down from heating and expansion. Uniform rotation in the convective zone leads to shear at its top with a discontinuous velocity of $\Delta V \sim 10^5$–10^6 cm s^{-1} at late times.

3.2.2. Outward Transport of Angular Momentum by Convection

The other rotation law that we consider is motivated by numerical simulations and observations of the Sun. In theoretical and numerical studies where Ro $\lesssim 1$, a generic feature is that angular momentum is transported outward away from the poles and toward the equator (Gilman 1979; Miesch 2000; Brun & Toomre 2002; Browning et al. 2004). This appears to be controlled by the largest scale eddies that are most influenced by rotation (Browning et al. 2004). Such features are qualitatively consistent with helioseismic measurements that map the outer convective region of the Sun (Thompson et al. 2003 and references therein). The main disparity is that theory and numerics generally result in a more Taylor-Proudman-like spin profile, whereas the Sun's velocity contours are more radial. This may be due to the tachocline (Miesch et al. 2006), which is present in cases with surface convection. The study of core convection in rotating A stars by Browning et al. (2004), who also find a Taylor-Proudman spin profile, may be the most relevant comparison to the WD case.

To mimic the general features of the spin profiles described above, we consider the following rotation law:

$$\Omega(r, \theta) = \left[\beta\left(\frac{r \sin\theta}{R_{\text{conv}}} \right) + 1 \right] \Omega_c, \qquad (30)$$

where Ω_c is the spin at the WD's center, β is the fractional change in spin across the convective zone, and θ is the latitude measured from the pole. For calculational purposes, we choose $\beta = 0.4$. This is in reasonable agreement with the results of Browning et al. (2004) and solar observations (Thompson et al. 2003), which both have a similar value of Ro ~ 0.1 in comparison to our case here.
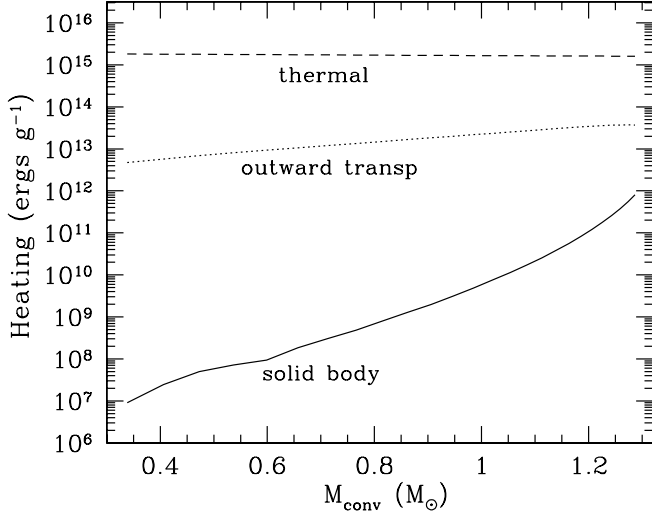
Fig. 9.—Heating available from the shear at the convective/nonconvective boundary as a function of the boundary's mass coordinate. These are found for both of the rotation laws we consider for the convection of solid body rotation (*solid line*) and outward angular momentum transport (*dotted line*). As a comparison, we show the thermal energy at the top of the convection zone, $c_p T$ (*dashed line*).

In Figure 8, we plot the spin profile along the equator using equation (30) as the rotation law within the convection. The outward transport of angular momentum is much more prominent than in the uniform rotation case considered earlier. Since the rotation is cylindrical, the shear is significantly smaller at higher latitudes. The typical velocity jump at the equator is $\Delta V \sim 10^6 - 10^7$ cm s^{-1}, which may be comparable to the speeds of the burning fluid elements that will be buoyantly rising through the WD once explosive carbon ignition occurs. This could, in principle, shear out the burning, enhancing it because of the increased surface area.

3.2.3. *Heating at the Convective Boundary*

The shear present at the convective/nonconvective boundary represents free energy that has been made available because of angular momentum transport by convection. If this shear persists throughout the convective stage, then it may have interesting effects on the subsequent flame propagation. The shear is not smeared out by convective overshooting. Using an overshooting length $L \approx V_{conv}^2/(2g)$ and a sound speed c_s, we estimate that $L/H \sim (V_{conv}/c_s)^2 \ll 1$, since the convective velocities are very subsonic. On the other hand, viscous processes may act at this interface, damping out the shear and leading to heating. Assuming that all of the shear is converted to heat gives a local heating per unit mass of $\sim (\Delta V)^2$. This is basically an upper limit of the energy generation rate at any given time.

In Figure 9, we plot the free energy per unit mass available from the shear at the convective/nonconvective boundary for both rotation laws. This is shown to be less than the thermal energy at the same location, $c_p T$. We note that these results are for an initial spin of $\approx 0.1 \Omega_K$ (chosen so that the spin would have minimal impact on hydrostatic balance). Since $\Delta V \propto \Omega$, the heating can be up to ≈ 100 times larger than what we estimate here. In the case where angular momentum is transported outward by convection, dissipation of shear may be able to heat the outer layers of the star. This may be an important effect for priming the thermal profile and expanding the WD before the flame propagates past.

4. DISCUSSION AND CONCLUSION

In this study, we have investigated the internal rotation profile for SN Ia progenitors, focusing on the stages of accretion and simmering. Since these progenitors are formed exclusively in binary systems, they contain an enormous amount of angular momentum. This is important for the WD structure and the subsequent flame propagation during the explosive burning of a SN Ia.

We compared three different mechanisms for angular momentum transport during the accretion phase. Either the baroclinic instability or the Tayler-Spruit dynamo will limit the shear to such low values that the Kelvin-Helmholtz instability cannot occur. We argue that the WD will have nearly uniform rotation, consistent with the results of Saio & Nomoto (2004). Our conclusion provides support to the study of Piersanti et al. (2003), which assumes rigid rotation for accretion WDs. It also argues for the relevance of the rigidly rotating explosion models of Dominguez et al. (2006).

This conclusion has important implications for extremely energetic SNe Ia such as SN2003fg (SNLS-03D3bb; Howell et al. 2006), which has been argued to originate from a super-Chandrasekhar WD (Jeffery et al. 2006). One well-known way to get a mass this high is via strong differential rotation (Shapiro & Teukolsky 1983 and references therein). If uniform rotation is required, the WD mass can only be increased by a few percent over the normal Chandrasekhar limit. We should also mention that just because the WD mass is higher, the chemical yields of the deflagration or detonation of a strongly differentially rotating WD will not necessarily match the high nickel mass needed for SN2003fg (Steinmetz et al. 1992; Pfannes 2006). For this reason, other interpretations have been suggested for this SN Ia (Hillebrandt et al. 2007).

The simmering phase is another opportunity for differential rotation to develop within the WD. This occurs due to heating and expansion as well as angular momentum mixing by convection. The full impact of the convection is hard to determine with certainty. Given the characteristic convective velocities, we expect Ro $\lesssim 1$; thus the influence of rotation cannot be discounted. We consider two rotation laws for the convective zone, a uniform rotation case and another case where the spin increases outward. In both cases, the most dramatic shearing appears at the convective/nonconvective boundary. This shearing may have an impact on the propagation of flames or bubbles, and in some extreme circumstances may hold enough free energy to alter the thermal profile of the nonconvective envelope.

Given the impact that rotation could potentially have for SNe Ia, the time appears ripe for including such effects in simmering and flame propagation calculations. Simulations such as those performed by Browning et al. (2004) are not yet able to reach the characteristic fluid parameters expected during the simmering stage (such as the Reynolds and Rayleigh numbers; see the summary in Woosley et al. 2004; Wunsch & Woosley 2004). Nevertheless, Ro ≈ 0.1 is well within reach, as has been shown by the simulations of Kuhlen et al. (2006). The biggest difficulty for the future will be following the secular evolution of the WD as the convective zone grows. Since the carbon burning is so temperature-sensitive, the majority of the evolution takes place at late times (see Figs. 7 and 8). This will help limit the duration that must be simulated.

REFERENCES

Acheson, D. J. 1978, Philos. Trans. R. Soc. London A, 289, 459
Almgren, A. S., Bell, J. B., Rendleman, C. A., & Zingale, M. 2006a, ApJ, 637, 922
———. 2006b, ApJ, 649, 927
Balbus, S. A. 1995, ApJ, 453, 380
Balbus, S. A., & Hawley, J. F. 1991, ApJ, 376, 214
———. 1992, ApJ, 400, 610
Barkat, Z., & Wheeler, J. C. 1990, ApJ, 355, 602
Bisnovatyi-Kogan, G. S. 2001, MNRAS, 321, 315
Browning, M. K., Brun, A. S., & Toomre, J. 2004, ApJ, 601, 512
Bruenn, S. 1973, ApJ, 183, L125
Brun, A. S., & Toomre, J. 2002, ApJ, 570, 865
Caughlan, G. R., & Fowler, W. A. 1988, At. Data Nucl. Data Tables, 40, 283
Chabrier, G., & Potekhin, A. Y. 1998, Phys. Rev. E, 58, 4941
Chamulak, D. A., Brown, E. F., Timmes, F. X., & Dupczak, K. 2008, ApJ, in press (arXiv:0801.1643)
Chandrasekhar, S. 1960, Proc. Natl. Acad. Sci., 46, 253
Couch, R. G., & Arnett, W. D. 1975, ApJ, 196, 791
Cumming, A., & Bildsten, L. 2000, ApJ, 544, 453
Denissenkov, P. A., & Pinsonneault, M. 2007, ApJ, 655, 1157
Domínguez, I., Piersanti, L., Bravo, E., Tornambé, A., Straniero, O., & Gagliardi, S. 2006, ApJ, 644, 21
Fricke, K. 1969, A&A, 1, 388
Fujimoto, M. Y. 1987, A&A, 176, 53
———. 1988, A&A, 198, 163
———. 1993, ApJ, 419, 768
Gilman, P. A. 1979, ApJ, 231, 284
Hansen, C. J., & Kawaler, S. D. 1994, Steller Interiors: Physical Principles, Structure, and Evolution (Berlin: Springer)
Hillebrandt, W., & Niemeyer, J. C. 2000, ARA&A, 38, 191
Hillebrandt, W., Sim, S. A., & Röpke, F. K. 2007, A&A, 465, L17
Höflich, P., & Stein, J. 2002, ApJ, 568, 779
Howell, D. A., et al. 2006, Nature, 443, 308
Iben, I. 1978a, ApJ, 219, 213
———. 1978b, ApJ, 226, 996
———. 1982, ApJ, 253, 248
Jeffery, D. J., Branch, D., & Baron, E. 2006, ApJ, submitted (astro-ph/0609804)
Kuhlen, M., Woosley, S. E., & Glatzmaier, G. A. 2006, ApJ, 640, 407
Kumar, P., Narayan, R., & Loeb, A. 1995, ApJ, 453, 480
Lesaffre, P., Han, Z., Tout, C. A., Podsiadlowski, Ph., & Martin, R. G. 2006, MNRAS, 368, 187
Lesaffre, P., Podsiadlowski, Ph., & Martin, C. A. 2005, MNRAS, 356, 131
Livio, M., & Pringle, J. E. 1998, ApJ, 505, 339

MacDonald, J. 1979, Ph.D. thesis, Cambridge Univ.
Miesch, M. S. 2000, Sol. Phys., 192, 59
Miesch, M. S., Brun, A. S., & Toomre, J. 2006, ApJ, 641, 618
Mochkovitch, R. 1996, A&A, 311, 152
Nandkumar, R., & Pethick, C. J. 1984, MNRAS, 209, 511
Nomoto, K. 1982, ApJ, 253, 798
Paczyński, B. 1972, Astrophys. Lett., 11, 53
———. 1983, ApJ, 267, 315
———. 1991, ApJ, 370, 597
Pfannes, J. M. M. 2006, Ph.D. thesis, Univ. Würzburg
Piersanti, L., Gagliardi, S., Iber, I. J., & Tornambé, A. 2003, ApJ, 583, 885
Piro, A. L., & Bildsten, L. 2004, ApJ, 610, 977
———. 2007, ApJ, 663, 1252
———. 2008, ApJ, 673, 1009
Piro, A. L., & Chang, P. 2008, ApJ, 678, 1158
Popham, R., & Narayan, R. 1991, ApJ, 370, 604
Riess, A. G., et al. 2004, ApJ, 607, 665
Saio, H., & Nomoto, K. 2004, ApJ, 615, 444
Salpeter, E. E., & van Horn, H. M. 1969, ApJ, 155, 183
Schatz, H., Bildsten, L., Cumming, A., & Wiescher, M. 1999, ApJ, 524, 1014
Shapiro, S. L., & Teukolsky, S. A. 1983, Black Holes, White Dwarfs, and Neutron Stars: The Physics of Compact Objects (New York: Wiley)
Sion, E. M. 1999, PASP, 111, 532
Spruit, H. C. 1999, A&A, 349, 189
———. 2002, A&A, 381, 923
———. 2006, preprint (astro-ph/0607164)
Stein, J., Barkat, Z., & Wheeler, J. C. 1999, ApJ, 523, 381
Stein, J., & Wheeler, J. C. 2006, ApJ, 643, 1190
Steinmetz, M., Müller, E., & Hillebrandt, W. 1992, A&A, 254, 177
Tayler, R. J. 1973, MNRAS, 161, 365
Thompson, M. J., Christensen-Dalsgaard, J., & Miesch, M. S. 2003, ARA&A, 41, 599
Townsley, D. M., & Bildsten, L. 2004, ApJ, 600, 390
Velikhov, E. P. 1959, J. Exp. Theor. Phys., 36, 1398
Weaver, T. A., Woosley, S. E., & Zimmerman, G. B. 1978, ApJ, 225, 1021
Woosley, S. E., Wunsch, S., & Kuhlen, M. 2004, ApJ, 607, 921
Wunsch, S., & Woosley, S. E. 2004, ApJ, 616, 1102
Yakovlev, D. G., Gasques, L. R., Afanasjev, A. V., Beard, M., & Wiescher, M. 2006, Phys. Rev. C, 74, 035803
Yoon, S.-C., & Langer, N. 2004, A&A, 419, 623
Zahn, J.-P. 1992, A&A, 265, 115
Zingale, M., & Dursi, L. J. 2007, ApJ, 656, 333